JOURNAL OF AIRCRAFT
Vol. 32, No. 1, January–February 1995

Aerodynamics of a Finite Wing with Simulated Ice

A. Khodadoust* and M. B. Bragg†
University of Illinois at Urbana–Champaign, Urbana, Illinois 61801

The flowfield about a semispan finite wing with a simulated leading-edge ice accretion is studied experimentally. The finite wing was tested in both a straight and swept wing configuration. Surface pressures, fluorescent oil flow visualization, and helium bubble flow visualization studies of the flowfield are reported. The presence of the simulated ice accretion produces a large leading-edge separation bubble which results in a global change of the pressure field, reduction of lift and increase in drag. Fluorescent oil flow visualization and pressure distributions from the centerline of the straight wing at low angles of attack show a predominantly two-dimensional flowfield on the wing's upper surface. Three-dimensional effects due to the tip-induced vortex and root-wall interaction become important at high angles of attack. Oil flow visualization shows that wall suction near the wing root drastically changes the flowfield near the root. The measured span loads on the straight wing compare well with the computational results when the endwall is properly modeled. The swept wing has a highly three-dimensional flowfield. Pressure distributions indicate higher lift near the root and lower lift near the tip. Helium bubble traces show a strong spanwise flow component on the swept wing. These results are in good qualitative agreement with Navier-Stokes calculations.

I. Introduction

ACCRETION of ice on the aerodynamic surfaces of an aircraft results in a reduced safety margin and poses a major threat to flight safety. This is in part due to accumulation of ice on the leading edge of the wing, which leads to a gross change in the cross-sectional geometry of the wing. The aerodynamic properties of the wing change to the detriment of the aircraft performance and flight safety. Understanding the adverse effects of ice accretion is of critical importance due to its implication for flight safety.

Adverse effects due to ice accretion on aircraft surfaces have been studied for a long time. The earliest wind-tunnel work in the U.S. probably dates back to 1938 when Gulick[1] tested an aspect ratio 6 wing in the Langley Full Scale Wind Tunnel with roughness used to simulate ice accretion. A 25% reduction in lift and 90% increase in drag were reported for the conditions tested. Construction of the Icing Research Tunnel (IRT) at the NASA Lewis Research Center in Cleveland, Ohio has allowed testing of aircraft components in carefully controlled icing conditions. Potapczuk and Berkowitz[2] recently completed a study of the Boeing 737-200 ADV wing section under simulated icing conditions. Changes in lift, drag, and pitching moment were documented with increasing accumulation of ice.

Use of simulated ice shapes has facilitated icing research in conventional wind tunnels. Ingleman-Sundberg et al.[3] tested a transport airfoil with slats and flaps to document the effect of five different ice shapes. Bragg et al.[4] tested a NACA 63_2-A415 airfoil section in the NASA IRT under simulated icing conditions in typical cruise conditions for a general aviation aircraft. Both actual and simulated ice accretion shapes were studied during this test. The measured pressure distributions on the ice shapes showed extremely severe adverse pressure gradients in this region of the flow. These measurements gave an indication of large regions of recirculating flow in the immediate vicinity of the ice shapes.

With the advent of modern techniques in computational fluid dynamics and the rapid growth of computational capabilities, several researchers in the field began addressing the problem of an airfoil in icing conditions. In order to document the flowfield of an airfoil with simulated ice shape and provide the means for the verification of the emerging computational results, Bragg and his co-workers have studied the flowfield of an airfoil with a simulated ice shape in detail.[5–15] They used a NACA 0012 airfoil section to study the effect of a simulated glaze ice accretion on the aerodynamic performance degradation due to icing. Pressure distributions, in addition to integrated lift, drag, and pitching moment were reported. Oil and smoke flow visualization, in addition to splitter-plate oil flow visualization, have also been used to document the shape and size of the separation bubble and its reattachment location downstream of the iced airfoil leading edge. The measured pressures and integrated aerodynamic coefficients compared favorably with Navier-Stokes predictions[16] and the interactive boundary-layer (IBL) method.[17]

Hot-wire and split hot-film measurements of the boundary-layer profiles on the iced model, in addition to total-pressure probe measurements on the clean baseline model, were also documented. Based on these measurements and subsequent detailed analysis, the existence of a large leading-edge separation bubble, extending well beyond 35% chord prior to stall, was verified.[15] Due to its global effect on the pressure distribution of the airfoil, the ice-induced separation bubble was identified as a bubble of the long type, as described by Tani.[18] Additionally, the state of the boundary layer prior to separation from the ice horns, qualified these bubbles as laminar separation bubbles. A data base of experimental information has been compiled on the aerodynamic performance of the iced NACA 0012 airfoil.[13,14] These data represent the most complete experimental measurements available for the NACA 0012 airfoil with a simulated glaze ice. Attention has since focused on the three-dimensional wing.

A semispan, reflection-plane, rectangular wing in the straight and swept positions has been used to study the effects of the simulated leading-edge ice accretion on the aerodynamic performance of a finite wing. The same simulated ice shape used in the earlier two-dimensional tests is used on the finite wing. Measurements from the semispan wing in the straight configuration can be compared to earlier results from the two-dimensional model, whereas measurements on the wing in the swept configuration will allow the study of the three-dimensional effects.

Received Aug. 13, 1993; revision received April 6, 1994; accepted for publication April 23, 1994.

*Postdoctoral Research Associate, Department of Aeronautical and Astronautical Engineering. Member AIAA.

†Associate Professor, Department of Aeronautical and Astronautical Engineering. Associate Fellow AIAA.

In this article, experimental measurements taken on the finite wing in straight and swept configurations are presented. Surface pressures on the finite wing, in addition to fluorescent oil flow visualization and helium bubble traces on the upper surface of the finite wing, will be presented. These data were taken in part for comparison to the Navier-Stokes calculations of Kwon and Sankar.[19,20]

II. Experimental Procedure

A. Wind Tunnel and Model

The data were acquired in two wind tunnels, both similar in shape and design. The helium bubble and surface oil flow visualization tests were conducted in the subsonic wind tunnel at the University of Illinois at Urbana–Champaign. The tunnel is of conventional design with approximately a 2.8- by 4.0-ft test section, 8 ft in length. The tunnel operates at speeds from 0 to 165 mph at Reynolds numbers of up to 1.5×10^6/ft. The tunnel is of open-return type and uses four turbulence screens and honeycomb in the settling chamber to reduce tunnel turbulence to approximately 0.07%. The surface and wake pressure measurements were acquired in a similar, 3.3- by 4.6-ft tunnel, at the Ohio State University.

The three-dimensional model used for this test is a semispan wing with a chord of 15.0 in. and a span of 37.25 in. when in the straight configuration, Fig. 1. The swept wing has a sweep of 30 deg and a span of 35.18 in. The large model chord length was chosen in order to provide the desired Reynolds number. Data are presented for low angles of attack, where results are not significantly affected by the tunnel walls. A NACA 0012 airfoil section was chosen to compare to earlier two-dimensional tests. The model consists of several components to allow wing sweep and to allow different simulated ice shapes to be tested through interchangeable leading edges. Two leading edges have been constructed for the model ahead of the 15% station, a NACA 0012 leading edge and the simulated glaze ice accretion.

The ice accretion used is a simulation of that measured on a NACA 0012 airfoil in the NASA Icing Research Tunnel (Fig. 2). The icing conditions were a freestream velocity of 130 mph, angle of attack of 4 deg, icing time of 5 min, volume median diameter droplet of 20 μm, LWC = 2.1 g/m^3, and a temperature of 18°F.

The model is equipped with surface static pressure taps. The taps are located in 5 major rows plus a row on the tip section. The centerline row of taps has 80 taps in the no-ice configuration and 83 in the iced configuration. The other 4 rows on the main element have 40 and 41 taps in the no-ice and iced configurations, respectively. Including the 21 taps on the wing tip section, the model has a total of 261 taps in the no-ice configuration and 268 taps in the iced configuration.

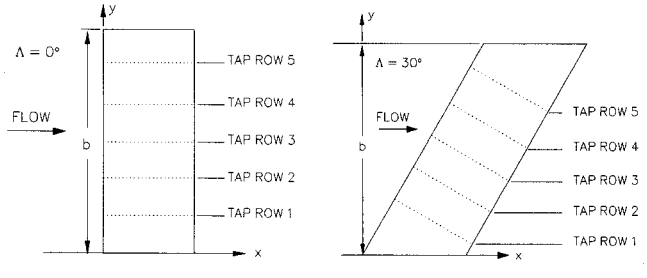

Fig. 1 Model coordinate system and measurement planes on the iced straight and swept wings.

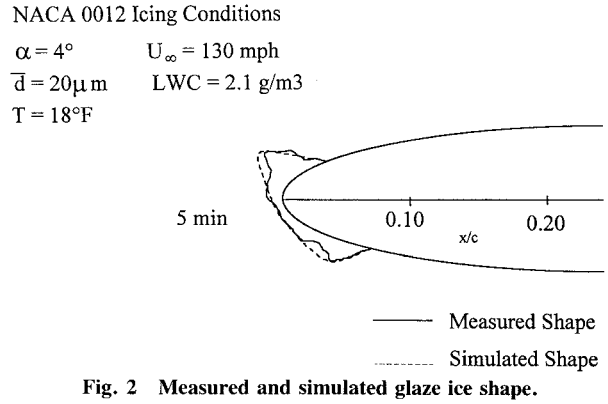

Fig. 2 Measured and simulated glaze ice shape.

B. Pressure Data Acquisition

Surface pressure measurements and facility pressures were taken using five 48-port Scanivalves. Model pressures were converted to pressure coefficients using the tunnel dynamic pressure measured on each of the Scanivalves. The pressure coefficients were then integrated to obtain the sectional lift coefficient. Note that when span loads are shown, Y is taken parallel to the leading edge and C_l is taken along the tap lines perpendicular to the leading edge. No tunnel wall corrections have been made to the surface pressure data.

The wake drag was measured by a total pressure probe behind the straight wing. The total pressure deficit, measured by the wake probe one chord length behind the model, was integrated to obtain airfoil section drag. The probe was placed halfway between tap rows two and three in order to minimize the effect of the pressure taps.

C. Sidewall Suction System

In order to minimize the effects of the sidewall boundary-layer interaction with the model, a boundary-layer suction system is employed (Fig. 3). An L-shaped suction plate in a circular turntable was mounted flush with the tunnel sidewall. The suction plate is perforated with a pattern of holes 0.0625 in. in diam in a staggered row pattern. It extends from 0.3 chord lengths upstream of the model leading edge to 0.9 chord lengths downstream of the model leading edge. Behind the plate, a plenum chamber leads through a 5-in.-diam PVC duct to a high-pressure blower. Suction rates are controlled by varying the blower speed through a variable frequency ac motor controller, mass flow through the duct is related through calibration to duct centerline dynamic pressure. The sidewall suction system is described in detail in Ref. 21.

D. Flow Visualization

Flow visualization was performed on the models using fluorescent oil. The oil is placed on the upper surface of the models and the tunnel is run until the flow pattern is established. The oil is illuminated with UV light and photographed with a 35mm camera. The oil flow visualization was performed at a chord Reynolds number of 1.2×10^6.

Helium-bubble flow visualization was conducted using a bubble generator. The bubbles are approximately $\frac{1}{16}$ in. in

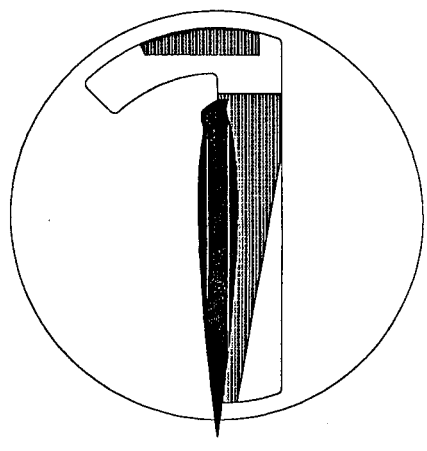

Fig. 3 Suction plate arrangement for the sidewall suction system.

diam, and are formed by injecting helium into a special soap film using a concentric injection tube arrangement. The helium-filled bubbles are approximately neutrally buoyant and able to follow the complex separated flows found in this study.[22,23] Two bubble generator heads producing a total of 800 bubbles/s were located in the tunnel settling chamber just aft of the antiturbulence screens. Photographs were then taken through a Plexiglas® window in the tunnel floor and the model was mounted inverted, upper surface down. The bubble paths were digitized using a motion analysis system.[23] The helium bubble flow visualization was performed at a chord Reynolds number of 6.5×10^5.

III. Results and Discussion

The results of measurements of model pressures, in addition to flow visualization data, are presented in the following sections. The results for the straight wing will be discussed first, followed by the results for the swept wing.

A. Straight Wing

Two-dimensional section data were taken on the three-dimensional straight wing using a single chordwise row of pressure taps and a wake probe traversing behind the section for drag. The sectional pressure measurements on the three-dimensional wing centerline is shown in Fig. 4. Also shown, is the pressure measurements from a similar but two-dimensional model.[12] The two pressure distributions are at similar lift coefficients and different angles of attack due to three-dimensional effects. Similar in size and shape to the two-dimensional pressure distribution, this sectional pressure measurement on the finite wing model clearly indicates the presence of a long separation bubble, as described by Tani.[18] The comparison is good in the leading-edge region, and downstream of pressure recovery, where the measured pressures are at nearly identical locations. The pressure recovery in the bubbles, which indicates reattachment,[18] are at slightly different locations, with the three-dimensional recovery being upstream of the two-dimensional recovery. This is in agreement with the integrated lift coefficients on the models, where the two-dimensional value is 5% higher than the sectional lift from the three-dimensional model. Analysis of the measurements on the two-dimensional model have shown very good correlation between pressure recovery and reattachment location.[15]

The measured pressure distributions indicate that the three-dimensional effects on the sectional properties are small at low lift coefficient. Pressure measurements and flow visualization at high angles of attack, discussed later in this article, show the three-dimensional effects becoming more significant as the stall regime is approached.

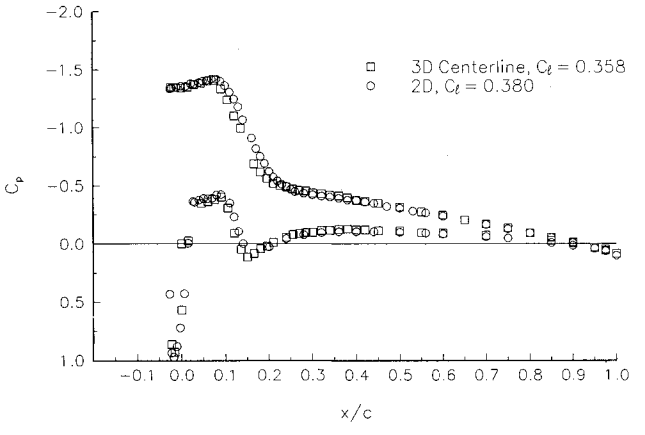

Fig. 4 Surface pressure distribution from the straight wing midspan compared to two-dimensional data. NACA 0012 with simulated ice, $Re = 1.5 \times 10^6$.

A comparison of the section drag polars from the two- and three-dimensional models, with and without simulated ice, is shown in Fig. 5. A large increase in drag is seen due to the presence of the simulated ice. The clean airfoil drag at zero lift was 0.0070, while the presence of the leading-edge ice accretion increased the drag to approximately 0.0250. The drag increase with angle of attack grows rapidly for the iced model due to the growth and eventual bursting of the leading-edge bubble. The comparison between the two-dimensional model and the section data from the three-dimensional model is quite good. The only significant deviation is at high angle of attack, where the drag for the clean three-dimensional model is somewhat higher.

Figure 6 gives a three-dimensional view of the surface pressures on the wing. At constant wing angle of attack, the pressure coefficients are plotted for each row of taps from the root to the tip. Results shown in Fig. 6 are for the iced wing at 8-deg angle of attack. The trend here follows that of a wing with a rectangular planform. It is well known that a semispan wing with a rectangular planform and no twist stalls at the root first.[24] Due to the downwash distribution, the effective angle of attack near the tip is lower than that at the root of the semispan wing. The pressure distribution measured with the inboard row of pressure taps, $y/b = 0.17$, shows the largest lift of the five tap rows displayed. The outboard row of pressure taps, $y/b = 0.85$, shows the smallest lift among the five spanwise tap row locations. The straight wing is near stall at $\alpha = 8$ deg. The $y/b = 0.85$ section has less lift, and the upper surface separation zone is slightly smaller since the section is at a lower effective angle of attack.

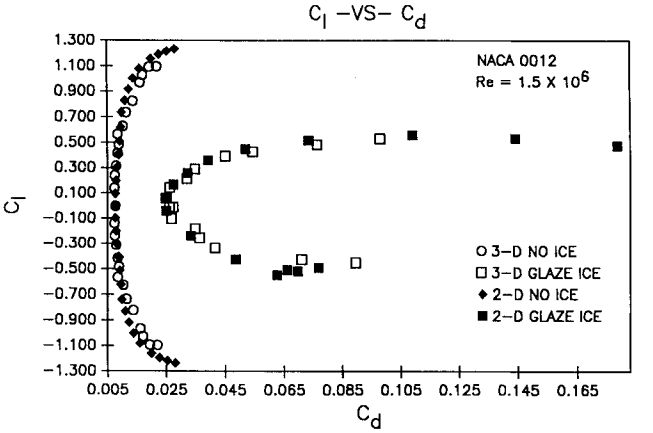

Fig. 5 Drag polar from the straight wing midspan with and without simulated ice compared to two-dimensional data.

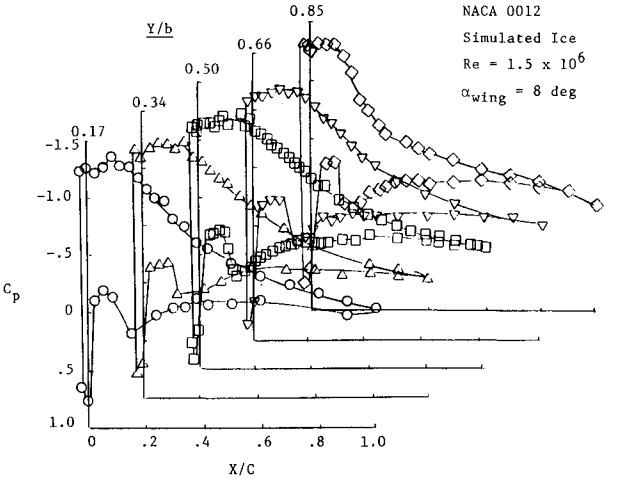

Fig. 6 Three-dimensional pressure distribution on the iced straight wing at $\alpha = 8$ deg, $Re = 1.5 \times 10^6$.

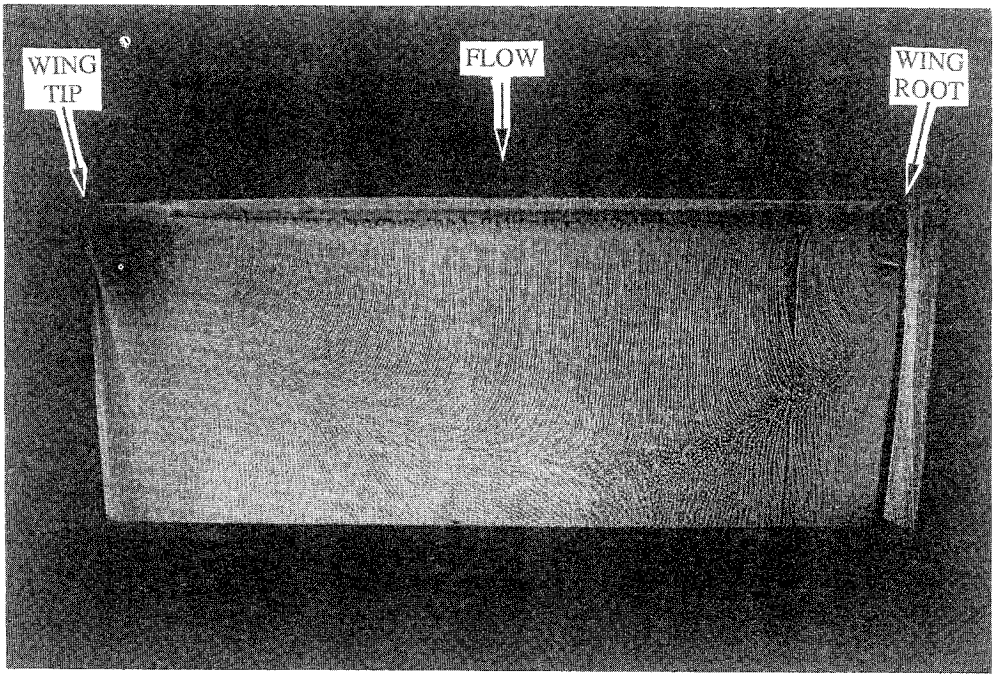

Fig. 7 Flow visualization on the iced straight wing with no suction applied, $\alpha = 8$ deg, $Re = 1.2 \times 10^6$.

The presence of the tunnel wall near the root of the semispan model can have a significant effect on the flow development in that region. Several researchers have examined the complex flowfield in the root-wall juncture.[25–29] The presence of the horseshoe vortex generated by the endwall flow separation upstream of the model leading edge, in addition to the boundary-layer growth on the tunnel wall, distort the flowfield from that which occurs at the center of a finite full-span wing. In the case of the semispan wing with simulated leading-edge ice, it is postulated that the interaction of the model and the wall in the experiment causes the separation bubble there to remain attached on the suction side to higher angles of attack than would be found with no wall present.[30]

The surface oil flow visualization on the iced straight wing with no suction is shown in Fig. 7 for $\alpha = 8$ deg and $Re = 1.2 \times 10^6$. The bubble reattachment line moves away from the wing leading edge very rapidly as we move from the model root to the model wingtip. Initially, near $x/c = 0.15$, the reattachment line reaches its maximum distance from the model leading edge ($x/c = 0.80$) near the wing midspan. The reattachment line gradually moves back towards the leading edge as the wingtip is approached. The reattachment line is closest to the leading edge near the model tip and root. The tip-induced vortex is the primary mechanism for the early reattachment of the separated flow in the tip region. The presence of the horseshoe vortex at the root-wall juncture is responsible for the early reattachment of the separated flow near the model root section.

A similar flow pattern has been obtained computationally on the iced rectangular wing.[20] The spanloads on the iced straight wing, calculated from the measured surface pressures, have been compared to those from three-dimensional Navier-Stokes computations.[30] In general, these comparisons are good. However, at 8-deg angle of attack the model-sidewall interaction is clearly seen in the experimental data. Figure 8 shows the experimental and calculated span loads for the iced straight wing at 4- and 8-deg angle of attack. The CFD results at $\alpha = 8$ deg were performed with and without modeling the boundary layer on the tunnel wall/reflection plane. Note that near the wall the experiment finds more lift than the calculations with no-wall boundary layer modeled. By modeling the wall, the CFD code predicts the sidewall separation and the horseshoe vortex and predicts the larger lifts due to early reattachment of the bubble near the root.

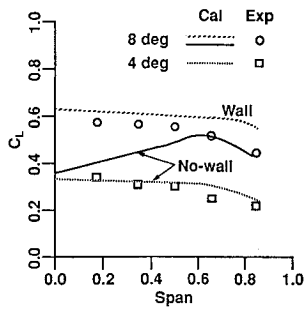

Fig. 8 Spanwise load distributions for the iced straight wing at $\alpha = 4$ and 8 deg. No-wall and wall boundary condition used.

Suction on the tunnel walls has been routinely utilized in wind-tunnel experiments. By varying the amount of suction, and therefore, the amount of mass removed from the wall boundary layer in the vicinity of the model, it is possible to remove the effect of the tunnel wall. Paschal et al.[31] conducted a series of tests in the Langley Low Turbulence Pressure Tunnel on a two-dimensional airfoil at high angles of attack. By applying suction at the tunnel wall upstream of the model as well as along the model upper surface, they were able to minimize the contamination effects of the wall boundary-layer separation at high angles of attack. The optimal suction configuration produced near uniform pressures across the span. In wind-tunnel experiments involving semispan wings, the application of suction at the wall can cause the flow pattern to change considerably near the root. During tests on a semispan wing, Bippes and Turk[25] applied suction at the tunnel wall for a strut-mounted semispan rectangular wing. At high angles of attack, their suction system changed the flowfield at the root-wall juncture, but was unable to produce a symmetric flowfield about the model root.

In order to examine the effect of the wind-tunnel wall boundary layer on the flowfield in the root region of the straight wing with the simulated leading-edge glaze ice, the sidewall suction system described in the previous section was utilized to remove the boundary-layer mass upstream and above the model surface. Figure 9 shows the same wing as in Fig. 7, but with wall suction applied at the root. Here, the suction coefficient C_s is defined as a percentage of the tunnel mass flux. It indicates the amount of mass removed from the

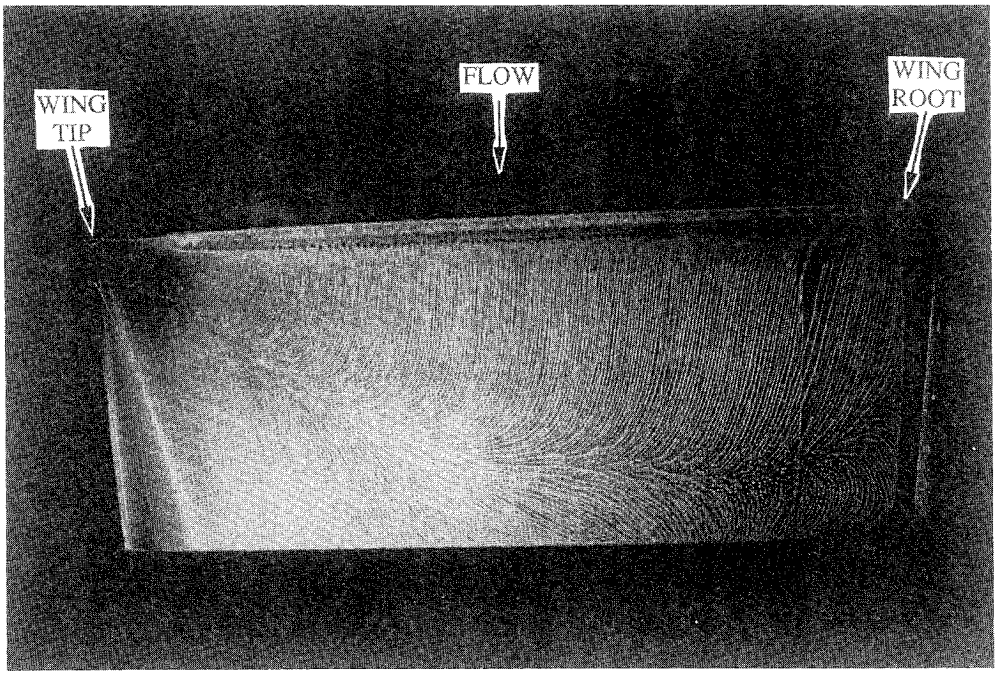

Fig. 9 Flow visualization on the iced straight wing with suction applied, C_s = 0.27, α = 8 deg, Re = 1.2 × 10⁶.

tunnel wall boundary layer.[21] Near the model root, the reattachment line appears in a different location than the case with no suction. Moving from the root towards the tip, the reattachment line departs from the model root at approximately x/c = 0.60. Further outboard, the reattachment line extends to approximately x/c = 0.80, until just past the wing midspan where it begins a gradual approach towards the model leading edge. Note that the reattachment line shown in Fig. 9 is not necessarily the actual flow pattern on the semispan of an equivalent finite wing in free air. It merely points out that, with the proper amount and distribution of suction applied at the root, it should be possible to obtain the correct flow pattern. More experimentation with the sidewall suction system would be required before the proper suction setting for a particular angle of attack could be determined. The measurements performed on this rectangular semispan wing have been used to validate the CFD modeling of the same flowfield. By modeling the tunnel wall in the CFD formulation, computational results have compared well with results from the no-suction experimental configuration. Since aircraft experience this type of interaction in the wing/fuselage juncture, and due to the complexity and uncertainty in setting a sidewall suction system to simulate the free-air case, data taken for CFD comparison was with a well-documented, no-sidewall-suction configuration.

B. Swept Wing

The character of the flowfield is quite different on the swept wing. As the results from surface oil flow and helium bubble flow visualization suggest, the flowfield on the swept wing is highly three dimensional. The results from the three-dimensional Navier-Stokes computations also lead to the same conclusion.

The CFD particle traces are shown in Figs. 10 and 11 for α = 4 and 8 deg, respectively. The location of several massless particles is tracked over the wing in order to render the image shown in Figs. 10 and 11.[30] The α = 4-deg case clearly shows the formation of a leading-edge vortex. This vortex forms in the separation bubble aft of the upper surface ice horn. The vortex grows in diameter as it moves out from the root to the tip. Spanwise velocities in the vortex are seen to be quite large.[19] Also note that significant spanwise flow is seen aft of the leading-edge vortex, particularly in the reattachment region.

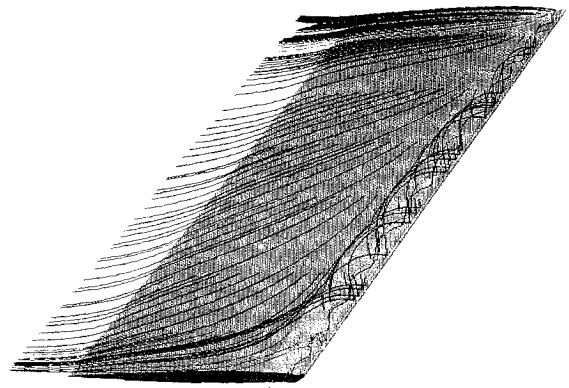

Fig. 10 Off-body particle traces for the iced swept wing at α = 4 deg, Re = 1.5 × 10⁶.

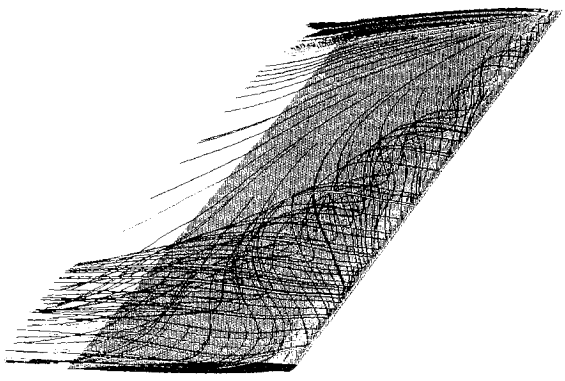

Fig. 11 Off-body particle traces for the iced swept wing at α = 8 deg, Re = 1.5 × 10⁶.

The CFD particle-trace flow visualization shows a complex flowfield for the iced swept wing at α = 8 deg. The leading-edge separation bubble seen at α = 4 deg has now enlarged significantly. The massless particle traces in the separation bubble show a large region of recirculation, growing rapidly in diameter as the wingtip is approached. An indication of the spanwise flow on the swept wing's upper surface is seen from the particle traces downstream of the separation bubble

near the model root. This is partly due to the stall characteristics of a swept wing. A swept wing tends to stall at the wingtip first.[24,32] The CFD flow visualization shows a massively separated flow region on the swept wing starting near the wingtip and extending into the midspan region of the wing, creating a very complex flow pattern.

Similar conclusions can be drawn from fluorescent oil flow visualization. Figure 12 shows the surface oil flow pattern on the upper surface of the swept wing at $\alpha = 8$ deg and $Re = 1.2 \times 10^6$. Here, the vortex grows as it moves from the root to the tip. Ahead of this line, the vortex-induced surface flow is forward into the freestream and towards the tip. Near the tip the flow is essentially parallel to the trailing edge behind the reattachment line. The interaction of the large leading-edge vortex and the tip vortex cause the very complex flow pattern at the tip. The flow moves forward toward the leading edge, then turns back towards the trailing edge, all the time flowing outboard. Near the trailing edge this motion is more pronounced in the experimental data. The experimental data shows a somewhat different flow at the tip in the midchord to leading-edge region. This is probably due to the simpler leading-edge geometry used in the CFD model.[30]

The helium-bubble flow visualization technique gives experimental evidence of spanwise flow in the separation bubble region aft of the upper surface ice horn on the swept wing.[23] The bubble trajectories for the $\alpha = 4$-deg case, along with the computational reattachment line, are shown in Fig. 13, plotted on the semispan swept wing. The computational reattachment line has been deduced from Fig. 10. Here, the bubble trajectories show a motion corresponding to a vortex taking fluid from the root to the tip aft of the upper surface ice horn. Analysis of the high-speed motion video of the bubble trajectories indicated an average spanwise velocity that was 0.39 times the freestream magnitude.[23]

The experimental trajectories for the $\alpha = 8$-deg case are shown in Fig. 14. The boundary of the leading-edge vortex and the reattachment line deduced from the computational flow visualization shown in Fig. 11, is also shown here. The experimental trajectories appear to exhibit the same spiraling motion towards the tip as seen in the 4-deg case. Here, the leading-edge vortex grows in diameter as it moves from the root to the tip on the model upper surface. Analysis of the digitized bubble traces indicated an average spanwise velocity of 0.28 times the freestream magnitude. Note that the vortical flow region, as defined by the boundaries of the helium bubble trajectories, appears smaller than the same region as defined by the computational results. Due to the complex flowfield, the helium bubbles may not seed the entire vortex region.

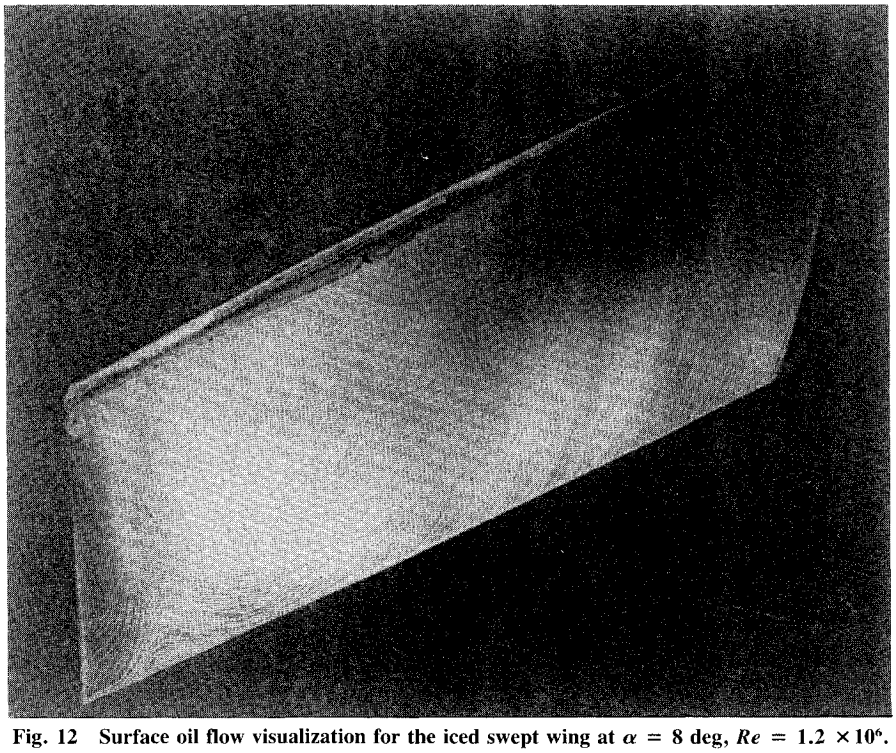

Fig. 12 Surface oil flow visualization for the iced swept wing at $\alpha = 8$ deg, $Re = 1.2 \times 10^6$.

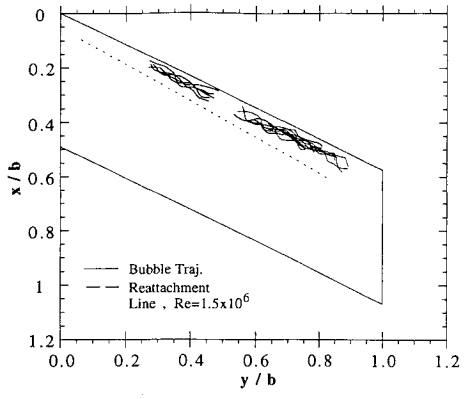

Fig. 13 Helium bubble trajectories for the iced swept wing at $\alpha = 4$ deg, $Re = 6.5 \times 10^5$.

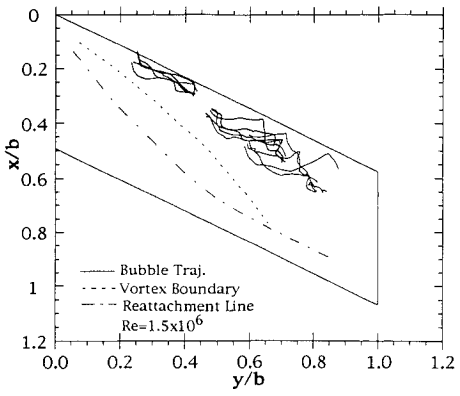

Fig. 14 Helium bubble trajectories for the iced swept wing at $\alpha = 8$ deg, $Re = 6.5 \times 10^5$.

The trends shown with the helium bubble trajectories, however, are quite clear and in general agreement with the numerical flow visualization.

Similar to the 4-deg case, here also the spanwise velocity in the separated, vortex-induced, flow has been reported to generally decrease as the wing outboard section is approached.[19] This is consistent with a vortex growing in diameter and becoming more diffuse as the wingtip is approached. Recent measurements with a laser Doppler velocimeter on the same wing have revealed significant spanwise velocities, exceeding twice the freestream, just above the model upper surface and downstream of separation in the shear layer.[33] The magnitude decreased in measurement planes further downstream and in the separation bubble, below the shear layer where maximum spanwise velocities on the order of 0.25–0.50 the freestream were typically seen.

The spanloads on the swept wing, calculated from the measured pressures, reveal the effects of leading-edge ice contamination on the aerodynamics of the swept semispan wing. These are shown in Fig. 15 for positive angles of attack. At low angles of attack, the wing loading is little affected by the presence of the ice shape. At $\alpha = 6$ deg and beyond, a noticeable reduction in the wing loading of the outboard sections of the wing is observed. This is a typical stall characteristic for a swept wing.[23,31] The presence of the simulated ice shape appears to promote the stall process.

The lift reduction in the outboard sections of the wing can also be examined through the pressure distributions directly. The measured pressures at the five tap rows on the iced swept wing are shown in Fig. 16 for $\alpha = 8$ deg and $Re = 1.5 \times 10^6$. The inboard tap row indicates a relatively short pressure plateau followed by rapid pressure recovery. Moving toward the tip, the measurements indicate a longer pressure plateau. This is an indication of the size of the separation bubble growing with spanwise distance. The pressure distribution shown for the outboard tap row ($y/b = 0.89$) is typical of an iced airfoil section that is very near stall.[7,9,12-14] Note that the inboard tap row ($y/b = 0.27$) shows the highest suction peak. Moving from the root to the tip, the peak suction decreases for each tap row with the outboard tap row indicating the lowest suction peak. A decrease in the suction peak in subsonic incompressible flow is analogous to a decrease in the velocity. Such a reduction in velocity has been measured with a laser Doppler velocimeter on the same wing.[33]

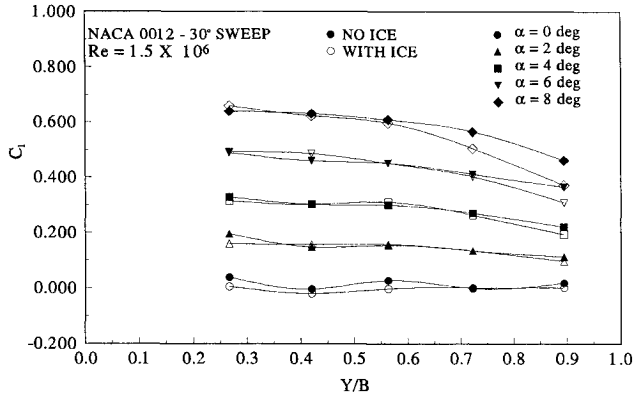

Fig. 15 Measured spanloads for the swept wing with and without simulated glaze ice, positive α.

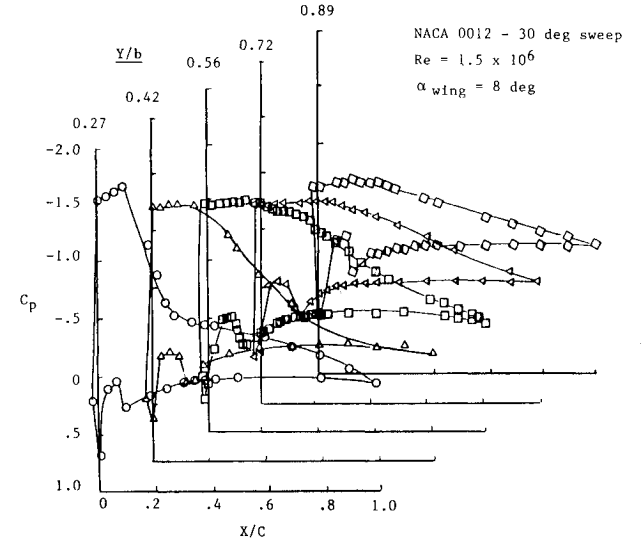

Fig. 16 Three-dimensional pressure distribution on the iced swept wing at $\alpha = 8$ deg, $Re = 1.5 \times 10^6$.

IV. Summary

The flowfield of a semispan wing with a simulated leading-edge ice accretion has been studied experimentally at $\alpha = 4$ and 8 deg. Large regions of separation due to the presence of the simulated ice shape are observed on both the straight and swept wings.

Measured pressure distributions on the centerline of the straight wing compared well with measurements on a similar two-dimensional model at low angles of attack. The drag, as measured by a wake probe behind the wing, showed a clear drag penalty in the presence of simulated ice, not unlike that measured on a similar two-dimensional airfoil. Three-dimensional effects became significant at high angles of attack. The flowfield on the wing root interacted with the tunnel wall boundary layer to significantly reduce the ice-induced separation. Fluorescent oil flow visualization results on the straight wing clearly demonstrated this interaction. Comparison of the measured spanloads on the straight wing with Navier-Stokes calculations showed good agreement between experiment and computation when the endwall was properly modeled in the computations.

The measurements on the swept semispan wing indicated a highly three-dimensional flowfield. The CFD particle traces from the Navier-Stokes computations clearly showed the formation of a leading-edge vortex in the separation bubble aft of the ice horn, with large spanwise velocities reported in the vortex.[19,20] The fluorescent oil flow visualization on the swept wing upper surface shows the growth of the leading-edge vortex from root to tip. The growth pattern is in good agreement with the CFD particle traces. The wingtip of the swept wing demonstrated a very complex flow pattern at high angles of attack. The differences between the computational and experimental flowfields in this region are probably due to the simpler wingtip geometry used in the computations. The helium-bubble flow visualization clearly showed the spanwise flow in the leading-edge vortex aft of the upper surface ice horn. The magnitude of the average spanwise velocities were qualitatively comparable with those measured with a laser Doppler velocimeter. The spanloads on the swept wing reveal the effects of leading-edge ice accretion on the flowfield of the semispan swept wing. At high angles of attack, a noticeable reduction in the wing loading of the outboard sections is observed. The presence of the simulated ice shape appears to promote the wingtip stall phenomenon on the swept semispan wing.

Data indicating transition location in the bubble has not been presented here. Recent LDV measurements,[34] however, have correlated the transition location in the bubble with turbulence intensity measurements in the immediate vicinity of the ice shape.

Acknowledgments

This work was supported in part by NASA Grant NAG 3-28 while the authors were at the Ohio State University, Columbus, Ohio, and NAG 3-1134 at the University of Illinois

at Urbana–Champaign, Urbana, Illinois. The oil flow visualization on the semispan wings was carried out by graduate students Steve Wells and Michael Kerho. The authors are indebted to Mark Potapczuk from NASA Lewis Research Center, Cleveland, Ohio, and Lakshmi Sankar from Georgia Institute of Technology, Atlanta, Georgia, for providing the computational data and their contributions to the understanding of these flowfields.

References

[1]Gulick, B. G., "Effects of Simulated Ice Formation on the Aerodynamic Characteristics of an Airfoil," NACA WR L-292, May 1938.

[2]Potapczuk, M. G., and Berkowitz, B. M., "An Experimental Investigation of Multi-Element Airfoil Ice Accretion and Resulting Performance Degradation," NASA TM-101441, Jan. 1989.

[3]Ingleman-Sundberg, M., Trunov, O. K., and Ivaniko, A., "Methods for Prediction of the Influence of Ice on Aircraft Flying Characteristics," Joint Rept. of the 6th Meeting of the Swedish-Soviet Working Group on Flight Safety, NASA Lewis Research Center, Rept. JR-1, Cleveland, OH, 1977.

[4]Bragg, M. B., Gregorek, G. M., and Shaw, R. J., "Wind Tunnel Investigation of Airfoil Performance Degradation Due to Icing," AIAA Paper 82-0582, Jan. 1982.

[5]Bragg, M. B., and Coirier, W. J., "Detailed Measurements of the Flow Field in the Vicinity of an Airfoil with Glaze Ice," AIAA Paper 85-0409, Jan. 1985.

[6]Bragg, M. B., Gregorek, G. M., and Lee, J. D., "Airfoil Aerodynamics in Icing Conditions," *Journal of Aircraft*, Vol. 23, No. 1, 1986, pp. 76–81.

[7]Bragg, M. B., and Coirier, W. J., "Aerodynamic Measurements of an Airfoil with Simulated Glaze Ice," AIAA Paper 86-0484, Jan. 1986.

[8]Bragg, M. B., and Spring, S. A., "An Experimental Study of the Flow Field About an Airfoil with Glaze Ice," AIAA Paper 87-0100, Jan. 1987.

[9]Bragg, M. B., and Khodadoust, A., "Experimental Measurements in a Large Separation Bubble Due to a Simulated Glaze Ice Accretion," AIAA Paper 88-0116, Jan. 1988.

[10]Spring, S. A., "An Experimental Mapping of the Flow Field Behind a Glaze Ice Shape on a NACA 0012 Airfoil," M.S. Thesis, Ohio State Univ., Columbus, OH, June 1987; also NASA CR-180847, Jan. 1988.

[11]Khodadoust, A., "A Flow Visualization Study of the Leading Edge Separation Bubble on a NACA 0012 Airfoil with Simulated Glaze Ice," M.S. Thesis, Ohio State Univ., Columbus, OH, June 1987; also NASA CR-180846, Jan. 1988.

[12]Bragg, M. B., "Experimental Aerodynamic Characteristics of an NACA 0012 Airfoil with Simulated Glaze Ice," *Journal of Aircraft*, Vol. 25, No. 9, 1988, pp. 849–855.

[13]Bragg, M. B., "An Experimental Study of the Aerodynamics of a NACA 0012 Airfoil with a Simulated Glaze Ice Accretion, Vol. I," NASA CR-179571, Jan. 1987.

[14]Bragg, M. B., "An Experimental Study of the Aerodynamics of a NACA 0012 Airfoil with a Simulated Glaze Ice Accretion, Vol. II," Univ. of Illinois at Urbana–Champaign, Dept. of Aeronautical and Astronautical Engineering Rept., Urbana, IL, June 1990.

[15]Bragg, M. B., Khodadoust, A., and Spring, S. A., "Experimental Measurements in a Large Leading-Edge Separation Bubble Due to a Simulated Airfoil Ice Accretion," *AIAA Journal*, Vol. 30, No. 6, 1992, pp. 1462–1467.

[16]Potapczuk, M. G., "Numerical Analysis of a NACA 0012 Airfoil with Leading Edge Ice Accretions," AIAA Paper 87-0101, Jan. 1987.

[17]Cebeci, T., "Calculation of Flow over Iced Airfoils," *AIAA Journal*, Vol. 27, No. 7, 1989, pp. 853–861.

[18]Tani, I., "Low-Speed Flows Involving Bubble Separation," *Progress in Aerospace Sciences*, Vol. 5, 1964, pp. 70–103.

[19]Kwon, O., and Sankar, L., "Numerical Study of the Effects of Icing on Finite Wing Aerodynamics," AIAA Paper 90-0757, Jan. 1990.

[20]Kwon, O. J., and Sankar, L. N., "Numerical Investigation of Performance Degradation of Wings and Rotors Due to Icing," AIAA Paper 92-0412, Jan. 1992.

[21]Wells, S. L., "The Effect of Sidewall Suction on the Aerodynamics of a Semispan Wing with Simulated Ice," M.S. Thesis, Univ. of Illinois at Urbana–Champaign, Urbana, IL, May 1992.

[22]Hale, R. W., Tan, P., Stowell, R. C., and Ordway, D. E., "Development of an Integrated System for Flow Visualization in Air Using Neutrally-Buoyant Bubbles," Sage Action, Inc., Rept. SAI-RR 7107, Ithaca, NY, Dec. 1971.

[23]Kerho, M. F., "A Study of the Accuracy of Neutrally Buoyant Bubbles Used as Flow Tracers in Air," M.S. Thesis, Univ. of Illinois at Urbana–Champaign, Urbana, IL, Jan. 1992.

[24]Hoerner, F. D., *Fluid Dynamic Lift*, Hoerner Fluid Dynamics, Brick Town, NJ, 1975.

[25]Bippes, H., and Turk, M., "Half Model Testing Applied to Wings Above and Below Stall," *Recent Contributions to Fluid Mechanics*, Springer-Verlag, New York, 1982, pp. 22–30.

[26]Kubendran, L. R., and Harvey, W. D., "Juncture Flow Control Using Leading-Edge Fillets," AIAA Paper 85-4097, Oct. 1985.

[27]Devenport, W. J., and Simpson, R. L., "Turbulence Structure near the Nose of a Wing-Body Junction," AIAA Paper 87-1310, June 1987.

[28]Kubendran, L. R., Bar-Sever, A., and Harvey, W. D., "Flow Control in a Wing/Fuselage-Type Juncture," AIAA Paper 88-0614, Jan. 1988.

[29]Chang, P., and Gessner, F., "Experimental Investigation of Flow About a Strut-Endwall Configuration," AIAA Paper 90-1541, June 1990.

[30]Potapczuk, M. G., Bragg, M. B., Kwon, O. J., and Sankar, L. N., "Simulation of Iced Wing Aerodynamics," *Proceedings of the Conference on Effects of Adverse Weather on Aerodynamics* (France), 1991, pp. 7.1–7.15 (AGARD-CP-496).

[31]Paschal, K., Goodman, W., McGhee, R., Walker, B., and Wilcox, P., "Evaluation of Tunnel Sidewall Boundary-Layer Control Systems for High-Lift Airfoil Testing," AIAA Paper 91-3243, Sept. 1991.

[32]Jones, R. T., "Effects of Sweepback on Boundary Layer and Separation," NACA TR 884, July 1947.

[33]Bragg, M. B., Kerho, M. F., and Khodadoust, A., "LDV Flowfield Measurements on a Straight and Swept Wing with a Simulated Glaze Ice Accretion," AIAA Paper 93-0300, Jan. 1993.

[34]Khodadoust, A., "An Experimental Study of the Flowfield on a Semispan Rectangular Wing with a Simulated Glaze Ice Accretion," Ph.D. Dissertation, Univ. of Illinois at Urbana–Champaign, Urbana, IL, Jan. 1993; also NASA CR-195301, April 1994.